Recreating a CFD Simulation of Acetylene Combustion in LVOF Flame Spraying

Michael Vogl, Janardhanraj Subburaj, Touqeer Kashif, Aamir Farooq

1. Introduction

Flame spraying is a widely used coating process in industries such as aerospace, automotive, and energy to improve surface properties like wear and corrosion resistance. The process is generally divided into low-velocity oxy-fuel (LVOF) and high-velocity oxy-fuel (HVOF) spraying. In LVOF, particle velocities typically range from 15–30 m/s with flame temperatures around 3000–3400 K, while HVOF reaches higher jet velocities and denser coatings.

In an oxy-fuel flame spray system, acetylene and oxygen are combusted to generate a high-temperature jet that heats and accelerates powder particles toward the substrate. The molten or semi-molten particles flatten and solidify upon impact, forming a coating or layered structure without melting the bulk substrate. Flame shape and stability are mainly controlled by the fuel-to-oxygen ratio and gas flow rates, which define temperature, velocity, and residence time of the particles.

While acetylene is the conventional fuel for LVOF systems, our goal is to explore hydrogen as a cleaner alternative due to its carbon-free combustion and high thermal conductivity. This motivation underlies ongoing efforts to extend the validated acetylene-based models toward hydrogen-fueled flame spray systems.

2. Case Setup and Used Models

Our strategy is to first replicate the multireactional model presented in the validation study of Bandyopadhyay and Nylén (2003). Since that study compared simulation results directly with experimental measurements, reproducing their findings provides a solid baseline for our work. If our model in CONVERGE CFD reproduces the same gas flow, temperature, and particle data, we can assume the setup is correct. From this point, replacing acetylene with hydrogen as the fuel species allows us to extend the validated framework to study hydrogen combustion under otherwise identical conditions.

The computational domain is defined as a one-eighth wedge of the nozzle and surrounding flow field, exploiting the geometric symmetry of the system. This wedge includes a central orifice for the argon carrier gas, two fuel inlet holes from the total of sixteen around the nozzle rim, one cooling air inlet from the outer ring of nine orifices, and surrounding boundaries set to atmospheric conditions.

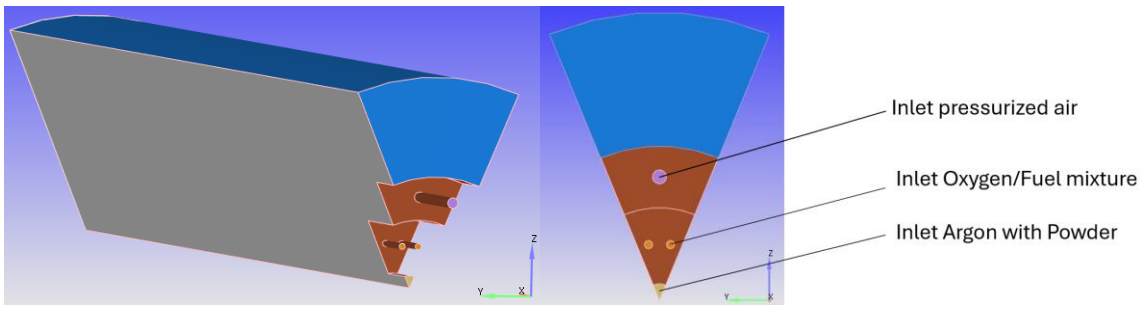

Figure 1: Domain in Converge CFD

This setup captures the essential physics while significantly reducing computational cost. Following the validation study, the nozzle wall is treated as adiabatic, periodic symmetry planes are imposed at the wedge boundaries, and the downstream outlet is set to atmospheric pressure. Within this framework, the multireaction chemical model is implemented to compare directly with the published reference data.

For the gas-phase chemistry, we employed input files derived from the GRI-Mech 3.0 mechanism. The chemical set includes the elements O, H, C, N, and Ar, with 53 species and 325 elementary reactions defined. The corresponding *mech.dat*, *thermo.dat*, and *transport.dat* files were implemented in CONVERGE to enable mixture-averaged transport properties. The Redlich–Kwong equation of state was chosen to account for real-gas effects at high temperatures and pressures. Combustion was modeled using the SAGE detailed chemistry solver, which directly integrates the reaction mechanism to resolve species concentrations and heat release rates.

For the particle phase, the validation study describes a composite structure with a bentonite core and a NiCrAl surface layer. In our simulation this was simplified to a homogeneous material composition of 70% Ni, 22% bentonite, 5% Al, and 3% Cr by weight. Convective heat transfer was modeled with the Ranz–Marshall correlation, while particle drag was represented using the Haider–Levenspiel model with a sphericity factor of 0.1 to approximate the irregular particle shapes reported in experiments. The particle size distribution was accounted for

Table 1: Gas flow rates and velocity

Gas stream	Inlet velocity [m/s]	Volume flow [lpm]
Argon (carrier gas)	12.6	6
Acetylene (C_2H_2)	117.4	22.9
Oxygen (O_2)	117.4	32
Cooling air	200	–

Table 2: particle size distribution

Particle diameter [µm]	Volume fraction [%]
30	5
65	28
105	48
165	20
265	2

Key Process Parameters

The flame spray process depends on several coupled parameters that control flame behavior, particle heating, and coating quality. Key factors include the fuel/oxygen ratio, which sets flame temperature and oxidation potential, and the gas flow rates, determining jet velocity and particle residence time. Particle size, feed rate, and powder material properties influence melting and solidification, while mass loading affects local flame temperature. Stand-off distance and spray angle govern particle impact conditions and coating uniformity, whereas nozzle design and gas thermal properties shape the overall flame structure and heat transfer. Proper adjustment of these variables is essential for reproducible simulations and experiments.

Even though process parameters of the powder were thoroughly looked at in the validation study, we mainly focused on the gas characteristics.

Reaction Mechanisms:

The study first applies a single-reaction global model ($2\ C_2H_2 + 5\ O_2 \rightarrow 4\ CO_2 + 2\ H_2O$) with the Eddy Dissipation model to capture the mixing-limited character of acetylene–oxygen combustion. In a second step, they introduce a multi-reaction mechanism using 22 reversible elementary reactions to resolve radical species and achieve more detailed flame structure and temperature predictions. We are only recreating the multi-reaction model with the more detailed version from GRI-Mech 3.0. The CFD solver requires three separate input files:

- mech.dat – the chemical reaction mechanism (global or multi-step).
- thermo.dat – NASA polynomial data for cp(T), h(T), and s(T) of all participating species.
- transport.dat – transport properties (collision diameters, potential well depths, dipole moments, etc.) for the same set of species.

Together, these files ensure consistent thermodynamic and transport modeling across the simulations. They were shortened from existing files to make simulation faster.

Numerical Models:

Turbulence is represented with the standard k–ε RANS model with wall functions. The energy equation is solved, with radiation disabled in the baseline but available later. For higher particle loadings, **two-way coupling** is applied to capture particle back-effects on gas flow and temperature.

Simulation Procedure:

Our workflow started with gas-phase simulations, focusing on reproducing the temperature and velocity fields reported in the validation study. Once the gas phase was established, particles were introduced to analyze heating, melting, and trajectories. This stepwise approach—from a simplified global model toward more detailed chemical and physical representations—was designed to ensure numerical stability and a meaningful comparison with experimental data.

The simulated temperature fields show good agreement with the reference study, while the predicted velocities and species mole fractions deviate more noticeably, although the general trends are captured correctly. Extensive troubleshooting was carried out, including testing different reaction mechanisms (such as the 22-reaction set used in the original study) and

turbulence–combustion models. Despite applying the same setup, identical results could not be reproduced. Additional efforts included testing various drag models for the particles and running both steady-state and transient cases. These tests yielded consistent results that remained slightly above the values reported in the validation study. Ultimately, the focus was placed on reproducing the overall trends rather than achieving exact numerical agreement. Future work could include implementing the single-reaction model, which would require determining or calculating the reaction coefficients (A, n, and Ea) for the global acetylene–oxygen reaction.

3. Results

Table 2 presents a direct comparison of predicted gas velocity and temperature profiles. The results obtained from the current simulation are depicted in red, while the reference data from the multireaction model of the validation study are shown in black. This initial comparison focuses on replicating the numerical model from the reference paper, which is a necessary and logical precursor to the subsequent validation against experimental data. By first ensuring that the computational model itself is accurately reproduced, a solid baseline for evaluating further discrepancies against experimental measurements is established.

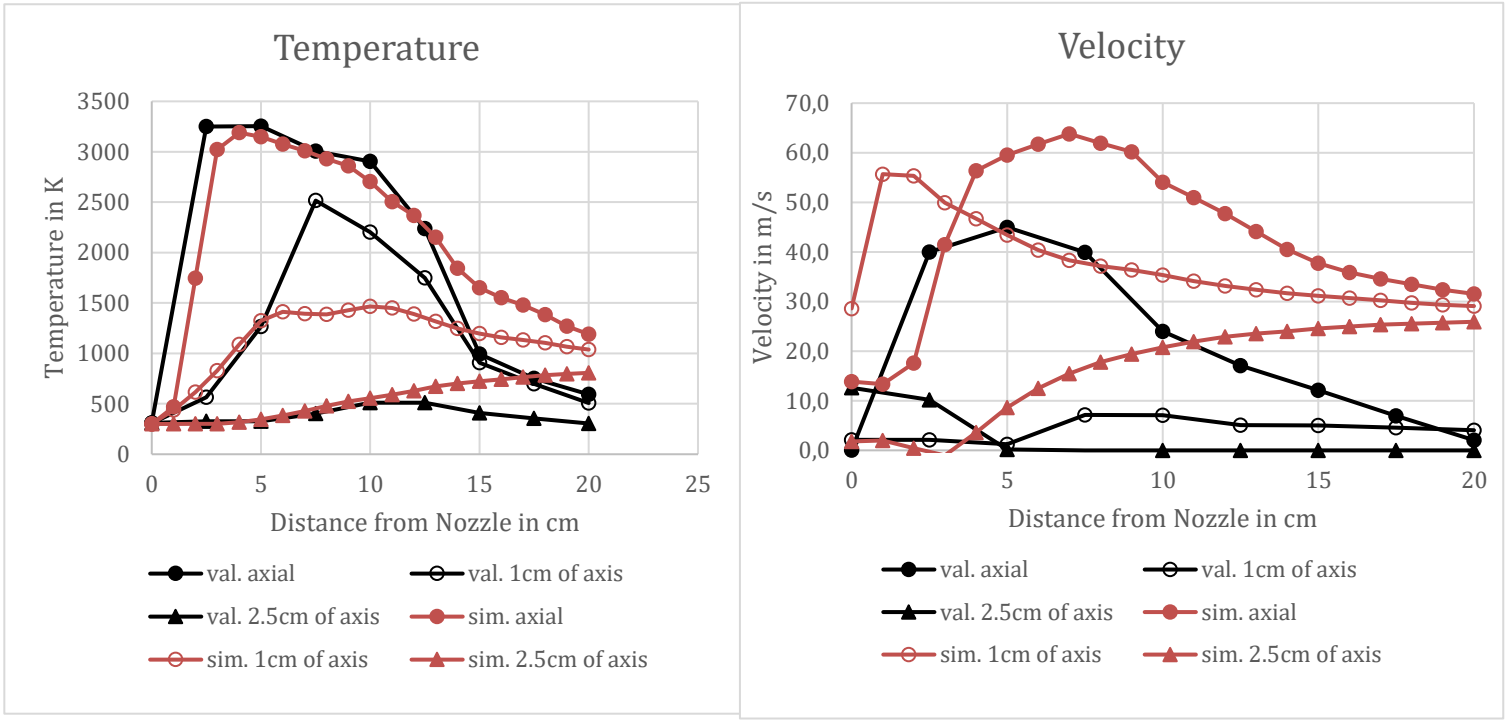

Figure 2: Simulated temperature and velocity of the gas from my simulation (red) and from the validation study (black)

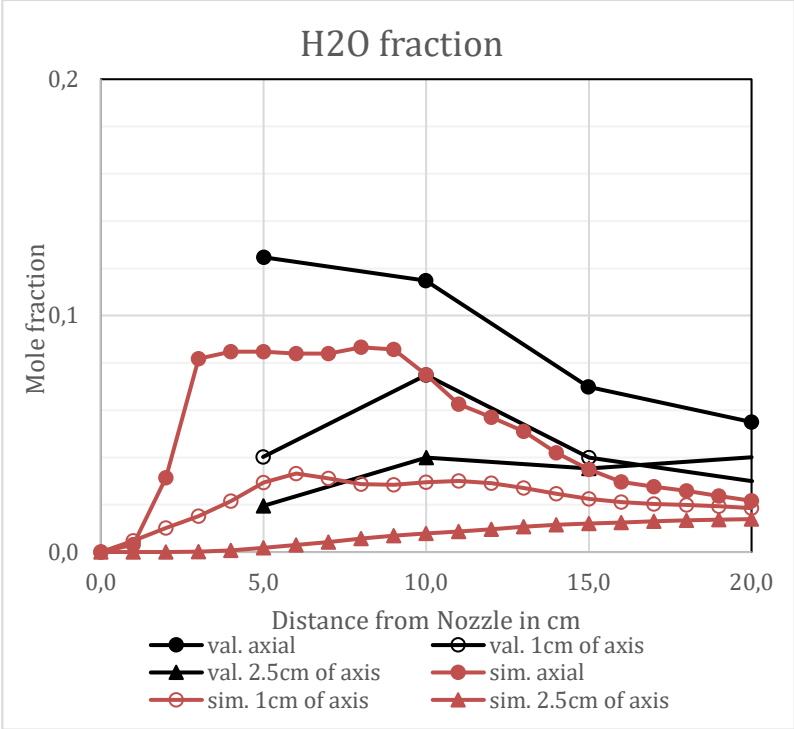

Figure 3: H2O mole fraction of my Simulation (red) and of the validation experiment (black)

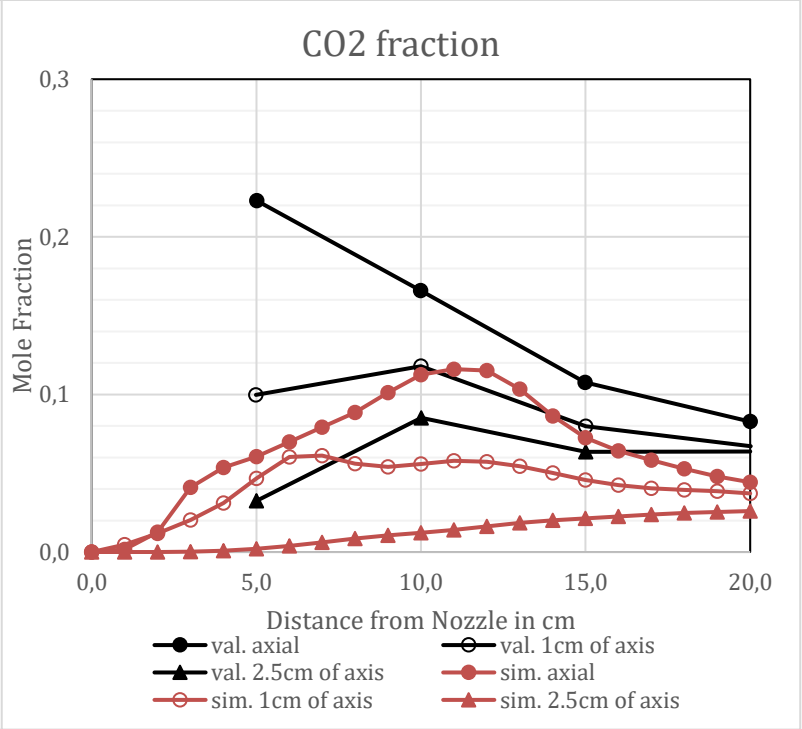

Figure 3: CO2 mole fraction of my simulation (red) and of the validation experiment (black)

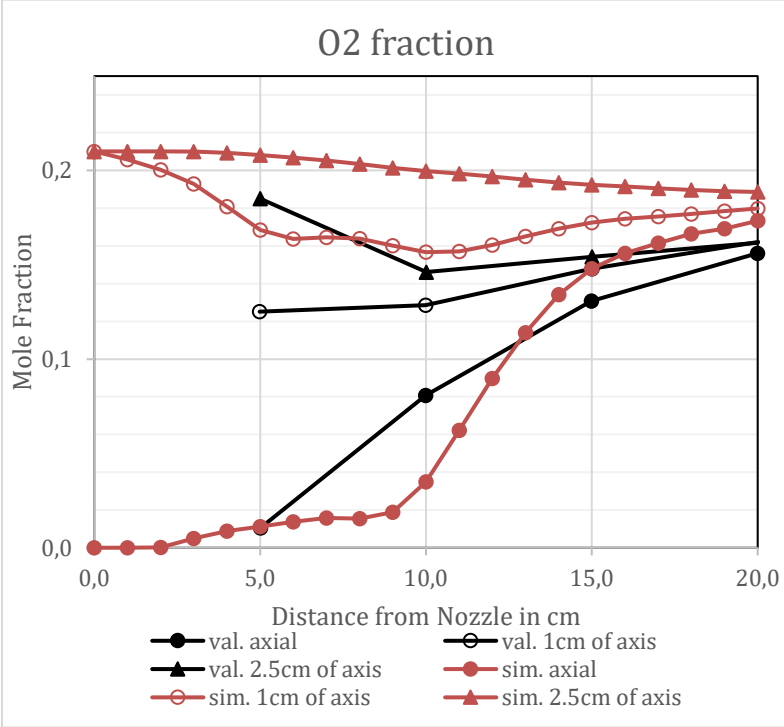

Figure 5: O2 mole fraction of my Simulation (red) and of the validation experiment (black)

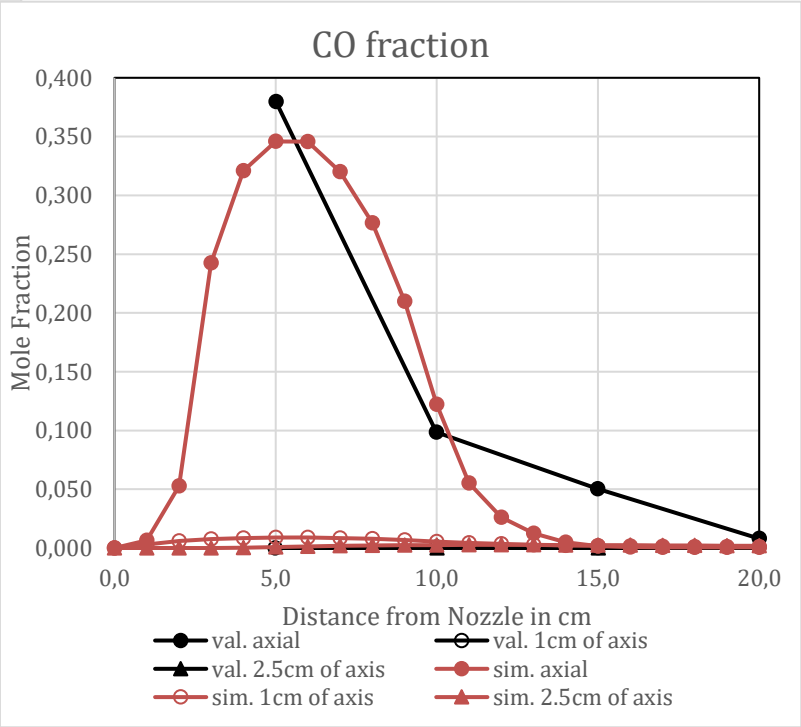

Figure 6: CO mole Fraction of my simulation (red) and of the validation experiment (black)

Figures 3-6 compare the mole fractions of various gas species along three distinct measurement lines. The results of the current simulation (red) are validated against experimental data (black) from the reference study, which were acquired using a DPV2000 optical system.

4. Discussion

Figure 2 compares the temperature profiles. Along the centerline, the simulation shows good agreement with the validation study up to an axial distance of 13 cm. However, more significant deviations are observed in the off-axis profiles. While the predicted temperature field is qualitatively plausible, this suggests that the close axial agreement might be coincidental, as a complete quantitative match with the reference data is not achieved across the entire domain.

Regarding the velocity field shown in Figure 2, a significant discrepancy is evident. The simulated velocities are consistently 20-40 m/s higher than those reported in the validation study. However, an analysis of the reference data reveals two apparent inconsistencies. First, the axial velocity at the nozzle centerline (0 cm) is reported as 0 m/s, which contradicts the specified argon carrier gas inlet velocity of 12.6 m/s. The current simulation predicts a more plausible 13.9 m/s at this location, consistent with the physical boundary condition. Second, the velocity profiles from the reference study exhibit a very rapid decay. This rate appears faster than what would be expected from momentum conservation in the gas flow. In contrast, the current simulation shows a more gradual velocity decay, which may be more physically representative.

When analyzing the mole fraction profiles, it must be noted that the experimental data consists of only four points per line, which may not fully resolve the concentration profiles, making a definitive trend analysis challenging. Nevertheless, the simulation qualitatively reproduces the trends for most species, which indicates a good degree of physical plausibility. The apparent decrease in the CO_2 concentration after the first measurement point at 5 cm is likely due to peak formation occurring very close to the nozzle, which was not captured in the measurements. Downstream of this peak, the concentration naturally decreases due to turbulent diffusion and the entrainment of surrounding air. A similar effect is visible in the O_2 profile, which correctly trends back towards the atmospheric concentration with increasing axial distance.

The concentration of carbon monoxide (CO) is highest along the centerline for two primary reasons. First, the centerline exhibits the highest temperatures, where the chemical equilibrium of CO_2 <=> CO + O shifts to favor the presence of CO. Second, this core region is often locally fuel-rich before sufficient oxygen from the ambient air is entrained, leading to incomplete combustion for which CO is a primary product. Generally, the simulation results show higher residual O_2 concentrations and lower CO_2 and H_2O concentrations compared to the validation data. This systematically indicates that the simulation under-predicts the overall extent of combustion. This discrepancy may stem from the turbulence-chemistry interaction, as the implemented finite-rate chemistry model might predict a slower reaction progress compared to the competitive finite-rate/eddy-dissipation model used in the reference study.

5. Literature

Bandyopadhyay, R., & Nylén, P. (2003). *A computational fluid dynamic analysis of gas and particle flow in flame spraying. Journal of Thermal Spray Technology, 12*(4), 492–503. https://doi.org/10.1361/105996303770348489

Mackie, J. C., Smith, J. G., Nelson, P. F., & Tyler, R. J. (1990). Inhibition of C_2 oxidation by methane under oxidative coupling conditions. *Energy & Fuels, 4*(3), 277–285. https://doi.org/10.1021/ef00021a011

Westbrook, C. K., & Dryer, F. L. (1981). Simplified reaction mechanisms for the oxidation of hydrocarbon fuels in flames. *Combustion Science and Technology, 27*(1-2), 31–43. https://doi.org/10.1080/00102208108946970

Thermal Spray Society (ASM International). (2013). *Thermal Spray Technology White Paper.* Materials Park, OH: ASM International. Retrieved from https://tss.asminternational.org

Antonini, J. M., McKinney, W. G., Lee, E. G., & Afshar, A. A. (2014). Review of the physicochemical properties and associated health effects of aerosols generated during thermal spray coating processes. *Journal of Toxicology and Environmental Health, Part B: Critical Reviews, 17*(6), 325–346. https://doi.org/10.1080/10937404.2014.955903

Hall, A. C., Williamson, R. L., Hirschfeld, D. A., Roemer, T. J., Cook, D. J., Neiser, R. A., Mayer, A. J., Cates, J. W., Urrea, D. A., Beatty, D. E., & McCloskey, J. F. (1997). Process–microstructure–property relationships in powder flame-sprayed ceramic coatings. *Journal of Thermal Spray Technology, 6*(2), 185–192. https://doi.org/10.1007/BF02646310

Dasgupta, D., Pal, P., Torelli, R., Som, S., Paulson, N., Liberatore, J., & Stan, M. (2021). Computational fluid dynamics modeling and analysis of silica nanoparticle synthesis in a flame spray pyrolysis reactor. *Powder Technology, 388,* 622–635. https://doi.org/10.1016/j.powtec.2021.04.014

Zhao, X., Li, C., Jiang, H., Li, S., & Han, X. (2021). Mechanistic study on the influence of hydrogen fuel in high-velocity oxygen-fuel (HVOF) thermal spraying process. *Journal of Thermal Spray Technology, 30*(7), 1718–1734. https://doi.org/10.1007/s11666-021-01299-5

Fauchais, P., & Vardelle, M. (2010). Sensors in spray processes. *Journal of Thermal Spray Technology, 19*(4), 668–694. https://doi.org/10.1007/s11666-010-9474-5

Kim, D. Y., Lee, J. B., Jeong, C. H., Park, S. S., Jung, J. Y., Choi, H. J., Lee, J. H., & Lee, S. H. (2020). Effects of curvature on the flow characteristics and particle behavior in the flame spray process. *Journal of Thermal Spray Technology, 29*(5), 1032–1046. https://doi.org/10.1007/s11666-020-01048-7

Fauchais, P. L., Heberlein, J. V. R., & Boulos, M. I. (2014). *Thermal Spray Fundamentals: From Powder to Part.* New York, NY: Springer. https://doi.org/10.1007/978-0-387-68991-3

Tejero-Martín, D., Rezvani Rad, M., McDonald, A., & Hussain, T. (2019). Beyond traditional coatings: A review on thermal-sprayed functional and smart coatings. *Surface & Coatings Technology, 370,* 1–30. https://doi.org/10.1016/j.surfcoat.2019.02.014